Miner Deposita (2009) 44:329–342
DOI 10.1007/s00126-008-0226-y

ARTICLE

New thermochronologic constraints on the evolution of the Zaldívar porphyry copper deposit, Northern Chile

Eduardo Campos · Jan Wijbrans · Paul A. M. Andriessen

Received: 12 November 2008 / Accepted: 30 November 2008 / Published online: 23 December 2008

Abstract Life spans and thermal evolution of hydrothermal systems are of fundamental metallogenic importance. We were able to establish the chronology and cooling history of the Zaldívar porphyry copper deposit (Northern Chile) by applying a combination of different isotopic dating methods in minerals with different closure temperatures, including $^{40}Ar/^{39}Ar$ geochronology and zircon fission track thermochronology, together with fluid inclusion thermometry and previous published U–Pb zircon geochronology. The hydrothermal mineralization in the Zaldívar deposit is genetically related to the Llamo Porphyry unit. Samples of igneous biotites from this intrusion yielded $^{40}Ar/^{39}Ar$ plateau ages between 35.5±0.7 and 37.7±0.4 Ma defining a weighted average of 36.6±0.5 Ma (2σ). In contrast, one sample from the Zaldívar porphyry, one from the andesites, and two from the Llamo porphyry yielded considerably younger fission track ages of approximately 29 Ma with a weighted mean for all ages of 29.1±1.7 Ma (2σ). Thermal and compositional constraints for the hydrothermal system in the Zaldívar deposit from fluid inclusions thermometry show that at least three fluid types broadly characterize two main hydrothermal episodes during the evolution of the deposit. The main mineralization and alteration event is characterized by high temperature (above 320°C) hypersaline fluids (salinity between 30 and 56 wt.% NaCl equivalents) coexisting with low-density gas-rich inclusions (salinity less than 17 wt.% NaCl equivalents) that homogenizing into the gas phase at temperatures above 350°C. The second episode corresponds to a low-temperature event which is characterized by liquid-rich fluid inclusions that homogenize into the liquid phase at temperatures ranging from 200°C to 300°C with salinities lower than 10 wt.% NaCl equivalents. The $^{40}Ar/^{39}Ar$ data (36.6±0.5 Ma, weighted average) obtained from igneous biotites represent the minimum age for the last high-temperature (above 300°C) hydrothermal pulse. When compared with previously published U–Pb ages (38.7±1.3 Ma) in zircons from the Llamo porphyry, a close temporal relationship between crystallization of the parental intrusion and the thermal collapse of the last high-temperature hydrothermal event is evident. Cooling took place from approximately 800°C (crystallization of the intrusive complex defined by zircon U–Pb ages) to below 300±50°C (biotite $^{40}Ar/^{39}Ar$ closure temperature) within approximately 1.5 m.y. Because the thermal annealing of fission tracks in zircons occurs at temperatures of 240±30°, the zircon fission track (ZFT) ages of 29.1±1.7 Ma (2σ) mark the end of the thermal activity in the Zaldívar area, specifically the time when the whole area cooled below this temperature, well after the collapse of the main hydrothermal event in the Zaldívar porphyry copper deposit. This cooling age roughly coincides with the age defined for the emplacement of dacitic dikes at 31±2.8 Ma (2σ) (published K–Ar whole rock), 5 km south of the Zaldívar deposit, in the Escondida area. This late magmatic pulse probably is responsible for high heat flow in the Zaldívar deposit as late as 29 Ma. There is no evidence that the low temperature hydrothermal pulse recognized by fluid inclusion studies is related to this thermal event. The zircon fission track

Editorial handling: P. Williams

E. Campos (✉)
Universidad Católica del Norte,
Avenida Angamos 0610,
Antofagasta, Chile
e-mail: edcampos@ucn.cl

J. Wijbrans · P. A. M. Andriessen
Vrije Universiteit Amsterdam,
De Boelelaan 1085,
1081 HV, Amsterdam, The Netherlands

cooling ages are interpreted to be related to the time lag required for complete relaxation of the perturbation of the isotherms in the geothermal field imposed by the intrusion of magmatic bodies, with or without any association with low temperature hydrothermal activity.

Keywords Porphyry copper · Thermochronology · Fluid inclusions · Chile

Introduction

Porphyry copper deposits result from large-scale intracrustal magmatic processes at convergent plate margins and the shallow emplacement (less than 6 km) of intermediate to felsic magmas. These processes lead to the generation of extensive hydrothermal systems that operate over a wide range of temperatures (~750°C to less than 200°C; see reviews by Richards 2003; Seedorff et al. 2005; Candela and Piccoli 2005). As the intrusions cool, the separation of volatiles during magmatic consolidation plays a fundamental role in the extraction and concentration of metals derived from the parental magma (e.g., Cline 1995; Campos et al. 2002; Proffett 2003; Williams-Jones and Heinrich 2005; Seedorff et al. 2005). The metal-rich fluids exsolved from the magma are then incorporated into early hydrothermal systems which are dominated by high-temperature high salinity magmatic fluids. In contrast, the late hydrothermal stages are dominated by low temperature, low salinity fluids thought to be the result of mixing of volatiles coming directly from the parental magma with waters of meteoric origin (e.g., Burham 1979; Fournier 1999; Cline 1995; Cline 2003; Harris et al. 2005).

To understand the genesis of hydrothermal ore deposits, knowledge of the life span and thermal evolution of the hydrothermal system is required. The purpose of the present study is to establish some constraints on the thermal evolution of the magmatic–hydrothermal system at the Zaldívar porphyry copper deposit (Northern Chile), starting with the crystallization of the Llamo porphyry intrusion and ending with the cessation of thermal activity by applying a combination of fluid inclusion microthermometry and a range of radiometric dating methods in minerals with different closure temperatures. The geochronological techniques applied in this study include fission track dating of zircon and $^{40}Ar/^{39}Ar$ biotite geochronology, as well as previously published U–Pb data (Richards et al. 1999). Hydrothermal systems are characterized by multiple superimposed fluid pulses that evolve from near-magmatic (>600°C) to considerably lower temperatures (<200°C; e.g., Titley and Beane 1981; Harris et al. 2003; Camus 2003; Proffett 2003; Harris et al. 2007). Thermal and compositional constraints for the major hydrothermal pulses that were active during the evolution of the hydrothermal system at the Zaldívar porphyry copper deposit were established by analysis of fluid inclusions.

Data from the application of multiple chronometers with different closure temperatures to different minerals whose isotopic systems have not been modified by subsequent alteration events have successfully been combined with microthermometric data. This allows to constrain the cooling history of ore deposits that are genetically related to magmatic systems associated to intense hydrothermal activity such as porphyry copper systems, e.g., El Teniente (Maksaev et al. 2004), Río Blanco (Deckart et al. 2005), and Bajo de la Alumbrera (Harris et al. 2007).

Geology of the Zaldívar deposit

The Zaldívar porphyry copper deposit is located in the Atacama Desert of Northern Chile, approximately 175 km SE of Antofagasta city (Fig. 1). The current proven and probable ore reserves are estimated at 421.3 million metric ton (Mt) at 0.67 wt.% Cu, equivalent to 2.83 Mt of copper. Current mine production is 146,000 tonnes of copper per year, which consists of 98% cathodes and the remainder as flotation concentrate (www.barrick.cl).

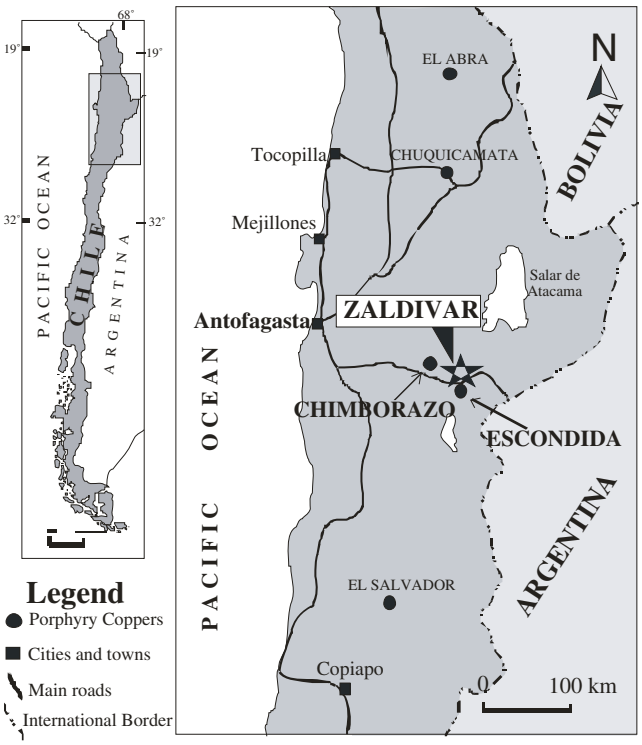

Fig. 1 Location map of Zaldívar porphyry copper deposit, also showing the Escondida, Chimborazo, and other Eocene to early Oligocene porphyry copper deposits

The Zaldívar deposit is part of a cluster of porphyry copper deposits which also includes the super giant (as defined by Cooke et al. 2005) Escondida deposit and the Chimborazo prospect (Fig. 1). The three porphyry systems are within the domain of the Domeyko Fault System, a crustal-scale NS-trending lineament, approximately 10 km wide and more than 1,000 km long. This Late Eocene–Early Oligocene structural belt controls the emplacement of major porphyry copper deposits in northern Chile (e.g., Chuquicamata, Collahuasi; Boric et al. 1990; Richards 2003; Gow and Walsh 2005). The porphyry magmatism at the Escondida and Zaldívar deposits was coeval at ~38 Ma (see below; Richards et al. 1999).

Three main lithological units are recognized at the Zaldívar deposit (Fig. 2). The most extensive igneous unit observed in the mine is the late Paleozoic Zaldívar porphyry (ZP), which crops out east of the NS-striking and near vertical dipping Portezuelo fault (Fig. 2). This rock is a coarse grained dacitic to rhyodacitic porphyry in which the phenocrysts (plagioclase, K-feldspar and quartz) are between 0.2 and 0.7 cm in size, in a fine-grained groundmass composed of feldspar, plagioclase, and quartz. The ZP is in faulted contact with andesitic lavas of the Augusta Victoria Formation, the latter cropping out to the west of the Portezuelo fault (Fig. 2). The andesites from the Augusta Victoria Formation were dated by Marinovic et al. (1995) between 66.6±2.2 and 41.2±2.2 Ma by K–Ar in biotites and whole rock. The lavas are greenish-gray to dark-gray in color, fine-grained to aphanitic, and, less commonly, with a fine-grained porphyritic texture. Where present, porphyritic rocks contain up to 30% of plagioclase phenocrysts, 0.1 to 0.2 cm in diameter, with a fine-grained, greenish- to brownish-gray groundmass composed of plagioclase, clinopyroxene, and hornblende.

The third rock unit is the Llamo porphyry (LLP), a light-gray/green dioritic to quartz-dioritic intrusion that represents the youngest recognized igneous rock in the mine. The LLP has an irregular NE–SW elongated shape and is between 50 and 200 m wide in plan view. It crops out on both sides of the Portezuelo fault (Fig. 2) and intrude the andesites of the Augusta Victoria Formation and the ZP (Fig. 2). This rock unit typically exhibits a medium-grained porphyritic texture with euhedral to subhedral phenocrysts smaller than 2 mm dominated by plagioclase, minor K-feldspar, biotite, and scarce quartz. Accessory minerals that occur disseminated in the groundmass include zircon and apatite. The groundmass represents less than 40 vol.% of the rock and comprises a fine-grained crystalline assemblage of feldspar, plagioclase, mafic minerals, and quartz. The Llamo porphyry at the Zaldívar deposit is assumed to have been emplaced during or immediately prior to ore deposition in the Zaldívar deposit (Richards et al. 1999; Campos et al. 2002) and is considered the intrusion most closely related to the mineralization and hydrothermal alteration.

Several hydrothermal and tectonic breccia bodies occur in the mine area closely associated with some major fault.

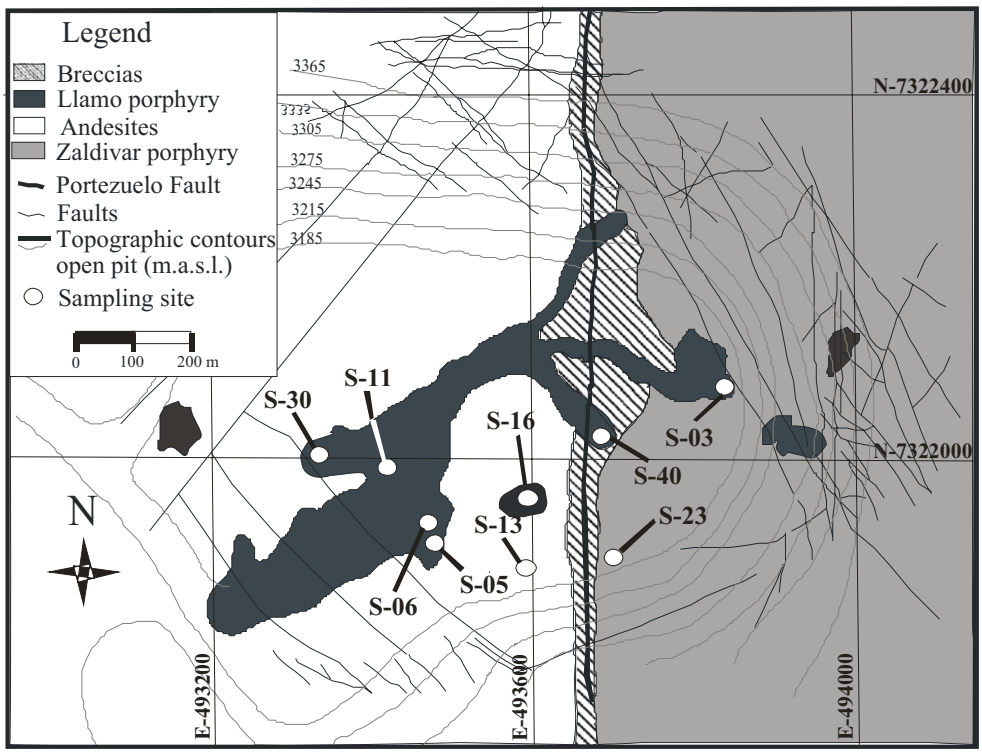

Fig. 2 Geology and sample location

These breccias commonly are discontinuous, monolithologic, clast-supported, and with angular clasts having the same composition as the surrounding rocks. In general, the breccia bodies are barren and not more than few tens of meters in diameter, with very few locations in which supergene copper mineralization occurs disseminated in the matrix.

The Zaldívar deposit is situated at the intersection of three major sets of faults that are described hereafter from oldest to youngest (relative ages are based on cross cutting relationships). A first fault set strikes N–S and dips steeply (70–85°) to the W; this fault set is only weakly to moderately developed but includes the major Portezuelo fault. The second set is the most dominant and includes numerous faults with a general NW–SE strike and steep dips (70° to 85°) to the NE or SW. This set is subparallel to the trend of the LLP and it may have controlled its emplacement (Fig. 2). The third fault set is poorly developed, strikes NE–SW, and dips moderately (50° to 65°) to the SE.

Hydrothermal alteration and mineralization

Different types of hydrothermal alteration assemblages modified the original mineral composition of all rock units present in the deposit. The earliest alteration event corresponds to a potassic mineral assemblage characterized by a selective replacement of plagioclase and ferromagnesian minerals by K-feldspar and secondary biotite, respectively, whereas primary K-feldspar and biotite remained unaffected. The potassic alteration is commonly overprinted by argillic alteration (kaolinite with minor sericite, chlorite, and quartz) that progress usually through microfractures into the phenocrysts and groundmass. The intensity of this argillic alteration varies from weak to pervasive. In the latter case, plagioclase crystals are completely replaced and only relics of the original mineral remain, whereas K-feldspar and biotite are less affected. Phyllic alteration (sericite–quartz–pyrite) is also present in the deposit, but it is weakly developed. Propylitic alteration mainly affects the andesites of the Augusta Victoria Formation, in the margins of the ore body. As the observed argillic alteration is spatially restricted to the leached cap described below and because neither K-feldspar nor biotite would have survived the physicochemical conditions at the advanced argillic or pervasive phyllic alteration zone (Titley and Beane 1981) and the biotite is readily converted to chlorite and clay minerals during intermediate argillic alteration (Einaudi 1998), the observed argillic alteration is supergene.

The copper mineralization at the Zaldívar deposit shows the typical supergene enrichment profile of copper deposits (e.g., Camus 2003), with a deep zone of hypogene sulfides that includes pyrite, chalcopyrite, molybdenite, and scarce bornite contained in quartz veins or as fine disseminations in all rock units cropping out in the lower levels of the mine. This hypogene mineralization is genetically linked to the hydrothermal system related to the LLP (Richards et al. 1999; Campos 2002). Supergene leaching of the hypogene ore has produced a leached cap that extends to a depth of about 150 m below the present surface and contains limonites, remnants of primary sulfides (mainly pyrite), and traces of copper oxides. The leached cap is underlain by the main ore body, a subhorizontal blanket of supergene mineralization between 100 and 150 m in thickness, and about 2 km long by 1 km wide, centered on the LLP. Two types of ore zones are recognized within this supergene blanket: (a) the Oxide Zone, where copper occurs principally as brochantite antlerite and chrysocolla and (b) the Sulfide Zone that includes chalcocite, covellite, and minor relict chalcopyrite (Maturana and Zaric 1991). The two ore zones are not distributed homogeneously throughout the deposit. In general, the oxidized minerals dominate in the andesites, whereas the supergene sulfides are most abundant in the intrusive units.

Previous geochronology

Only limited geochronologic data for the Zaldívar deposit has been published prior to this study. Richards et al. (1999) reported a U–Pb zircon age of 38.7±1.3 Ma from three zircon fractions that is interpreted as crystallization age for the LLP. The accuracy of U–Pb data reported by these authors failed to fit a regression line and returned imprecise lower and upper concordia intercepts of 39.1 and 298 Ma; these values are questionable as they were calculated by allocating equal weight to the analysis and zero error correlations. An alternative calculated concordia intercept using the concordant data from a different sample from a Paleozoic intrusion give a well-defined discordia line with upper and lower discordia intercept of 286±14 and 38.7±1.3 Ma, respectively. Despite all the uncertainties, 38.7±1.3 Ma is considered as a reasonable approximation to the crystallization age of the Llamo porphyry, in part supported by the timing of the cessation of the main magma-related high-temperature hydrothermal system. This is evidenced by a set of biotite $^{40}Ar/^{39}Ar$ cooling ages for the LLP of 37.4±0.2 Ma, using an incremental step-heating approach for argon release from relatively unaltered igneous biotite phenocrysts (Richards et al. 1999), for which Ar retention temperatures of 300±50°C are inferred (Harrison et al. 1985).

These constraints, overall, indicate a very short time interval between the crystallization of the syn-mineralization LLP and the cooling of the early hydrothermal alteration–mineralization event. Richards et al. (1999) concluded that

the magmatism observed in the three porphyry copper deposits situated within 15 km of each other (Zaldívar, Escondida, and Chimborazo) was coeval at approximately 38 Ma. They also suggested that a predominance of younger K–Ar dates (≤35 Ma) at Escondida deposit was caused by the disturbance or resetting effect on the K–Ar systems by the intrusion of a suite of dacitic dikes.

Several geochronologic studies have been carried out on the neighboring Escondida deposit (located only 5 km south from Zaldívar) that may also be useful in interpreting the ages obtained in the present study. According to Alpers and Brimhall (1988), hypogene alteration dated by the K–Ar method on biotite, sericite, and whole rock samples at Escondida occurred between 34.6±3.6 and 31.0±2.8 Ma. This dataset was subdivided into two groups corresponding roughly to potassic alteration (34–32.5 Ma) and phyllic alteration (from approximately 32.5 to 31 Ma). Furthermore, Zentilli et al. (1994) dated zircon crystals from a composite sample of the rhyolitic porphyry at Escondida, yielding an U–Pb age for magmatism of 32.6±2 Ma. Richards et al. (1999) and Padilla et al. (2004) dated the Colorado Grande and Escondida porphyries providing U–Pb crystallization ages for zircon at approximately 37 Ma. Nearly all K–Ar ages, mostly from whole rock samples reported by Ojeda (1986), fall within the 34 to 31 Ma range. The youngest date of 31±2.8 Ma (2σ) (Alpers and Brimhall 1988) was obtained from a late dacitic dike that crosscuts the rhyolitic porphyry.

Methodology

Samples

For $^{40}Ar/^{39}Ar$ geochronology, a total of seven samples from the LLP were collected from both sides of the Portezuelo fault (Fig. 2). Samples S-03, S-05, S-06, S-11, S-16, and S-30 are from a bench at 3,185 m a.s.l., whereas sample S-40 is from drill-core Z-112 taken at a depth of 3,115 m a.s.l. (Fig. 2). Samples S-05, S-06, S-11, S-16, S-30, and S-40 are magmatic biotite phenocrysts that occur mostly as dark-olive, hexagonal prisms less than 6 mm long with abundant mineral inclusions of feldspars, quartz, apatite, and zircon. The biotite crystals in sample S-03 are smaller and dark brownish in color, originated most likely by a later, localized, hydrothermal event.

Five samples were collected for fission track geochronology from bench 3155 in the Zaldívar open pit (300 m below original surface). Samples S-03, S-11, and S-30 are from the LLP, S-23 from the ZP, and S-13 is from an andesite of the Augusta Victoria Formation (Fig. 1). Fluid inclusion analyses were performed on quartz veins from the same sample set used for $^{40}Ar/^{39}Ar$ geochronology.

$^{40}Ar/^{39}Ar$ geochronology

Laser step heating experiments were carried out at the argon laser probe facility in the Laboratory of Isotopic Geology, Vrije Universiteit Amsterdam. The instrument consists of a 24-W CW argon ion laser, a low volume ultra-high vacuum gas inlet system, and a MAP 215-50 noble gas mass spectrometer. All isotopes were measured using a Johnston MM1 secondary electron multiplier (SEM) collector operated at a gain factor of 500 for the SEM over the Faraday cup at the highest setting. For a detailed description of the argon laser probe, see Wijbrans et al. (1995).

The rock samples were crushed to approximately 0.5 mm, and then individual biotite grains were hand-picked. All collected grains were washed in an ultrasonic bath for 1 min to avoid incorporation of material attached to the grain surface. Following the procedure described by Wijbrans et al. (1995), two of the freshest biotite grains from each sample were selected, loaded on aluminium sample holders, and irradiated during 7 h in the Cd-shielded position (CLICIT) at the TRIGA nuclear reactor at the Oregon State University at Corvallis, Corvallis, OR, USA.

After irradiation, samples were mounted in the sample tray and placed inside a stainless steel chamber connected to an ultra-high vacuum purification system. The sample chamber is positioned beneath a trinocular zoom microscope equipped with a video camera and a video monitor that allow observation of the sample. During incremental heating, argon extraction was performed by using a defocused continuous laser beam with a spot size of approximately 3 mm, sufficient to cover the whole sample and to ensure uniform heating of all grains from a given sample. During each analysis, biotite samples were heated in six heating steps of 1 min each with laser power settings between 0.3 and 1.4 W; a seventh step corresponds to the final fusion of the micas.

Each heating step was performed after 4 min of gas purification time. The evolved gas was admitted into the mass spectrometer where simple expansion ensures transfer of more than 90% of the argon for isotopic measurement. The gas was measured by stepping the magnet current at half mass intensity from 40 to 35.5 M/e. Blank intensities were measured routinely every four measurements, providing six blank analyses for every measuring day, allowing a good evaluation of argon blank intensities and reproducibility.

Fission track dating

Samples were crushed, pulverized, and washed to remove the fines. Subsequently, zircon grains were separated using

heavy liquids following the separation procedure described by de Bruijne (2001). After separation, zircon grains were mounted on a Teflon disk of about 20 mm diameter and polished. The polished grains were then etched in NaOH-KOH at 220°C for 96 h in order to obtain similar tracks for all zircon grains.

In this study, the external detector method (Fleischer et al. 1965) was applied for the fission track dating. In this method, a low-uranium mica sheet detector is placed in intimate contact with the etched surface of the zircon grains and is then irradiated in a nuclear reactor to create a set of induced tracks in both the zircon grains and in the mica. The induced tracks are produced by the fission of ^{235}U during the irradiation with thermal neutrons. After irradiation, the external detector is removed from the sample and etched. The uranium content of the sample is determined by counting the induced tracks in the mica sheet detector, and the flux of thermal neutrons is monitored by two dosimeter glasses of known uranium content that are included in the same package that contains the samples to be irradiated. The samples were irradiated for 3 hours in the low-flux reactor at Petten, The Netherlands. The determination of the ratio of spontaneous versus induced tracks for each grain on each sample yields the single grain ages (see Tagami 2005 for full review of method).

Several grains are counted (in this study between 20 and 25) to obtain the final fission track age of each sample, and the fission track age for the whole sample is defined as the central age that corresponds to the weighted mean of each single grain age (de Bruijne 2001). Graphically (see Fig. 6), the age for each counted grain age is determined by tracing a line from the origin through a given point and into the curved axis, whereas the central age is represented by a horizontal line extrapolated from the origin to the curved axis, with its standard error determined by two parallel lines at a distance of 2σ (Galbraith 1990).

Fluid inclusions thermometry

The observed fluid inclusions were classified according to their phase relations observable at room temperature, following the classification schemes of Roedder (1984) and Moore and Nash (1974). Conventional heating/freezing procedures on fluid inclusions were carried out with a Linkam TP/91-THMS 600, nitrogen-cooled stage (working temperature range −200°C to 600°C), assembled on an Olympus microscope. Temperature measurements were calibrated at low temperature using natural fluid inclusion samples with known phase transitions at −56.6°C (triple point of CO_2) and at 0.0°C (triple point of pure H_2O). Freezing rates varied between 50°C and 30°C/min.

Results

$^{40}Ar/^{39}Ar$ geochronology

The transformation of biotite to kaolinite caused by the supergene alteration varies from mild (sample S-03) with the alteration normally progressing inward or through microfractures as hairline veinlets interlaminated with the mica flakes to strong (sample S-30) where most biotites are totally replaced by fine-grained kaolinite (Fig. 3). Chlorite has been found only in samples S-05, S-06, and S-11, with the same mode of occurrence as kaolinite. Despite the susceptibility of biotite to supergene alteration, it was possible to collect grains that contain a fresh core suitable for $^{40}Ar/^{39}Ar$ geochronology from all selected samples.

Quantitative electron-microprobe analyses of selected biotite grains were carried out using a JEOL JXA-8800 instrument at the Vrije University Amsterdam. The analyses indicate that all biotite grains have K_2O content between 8 and 10 wt.% and X_{Mg} values between 0.61 and 0.71 (Table 1).

Plateau ages were defined when more than 50% of released ^{39}Ar was obtained from three or more contiguous heating steps. All errors shown on the age spectra represent analytical precision at 2σ and include the estimated error in the J value.

In sample S-30, about 70% of the argon gas was released in the first two heating steps and only 10% during final fusion of the biotite grains. The plateau for this sample is defined at 36.6±0.9 Ma (Fig. 4).

In samples S-16 and S-40, little ^{39}Ar was released during the first heating steps, and then plateaus are reached at 36.0±0.3 and 36.6±0.4 Ma, respectively. In both cases, more than 45% of the argon was released during the last fusion step (Fig. 4).

Samples S-06 and S-11 (Fig. 4) show a typical pattern of partial argon loss in the first heating step and then yielded good plateaus at 37.1±0.5 and 36.5±0.5 Ma, respectively. About 35% of the gas was released in the last two heating steps (Fig. 4). In sample S-05, the pattern indicates partial argon loss in the first two heating steps, which represent about 15% of the total ^{39}Ar gas released. The plateau is reached at 37.7±0.4 Ma (Fig. 4).

The hydrothermal biotites from sample S-03 also shows a typical pattern of partial argon loss in the first heating step representing about 18% of the total ^{39}Ar gas released and then a plateau is defined at 35.6±0.7. About 40% of the gas was released in the last two heating steps (Fig. 4).

To minimize the effect of outliers and to identify modes in the data that will lead to a better age determination, the $^{40}Ar/^{39}Ar$ ages were analyzed on a cumulative probability plot (Fig. 5). The plot for all the measured samples indicates that the most probable date

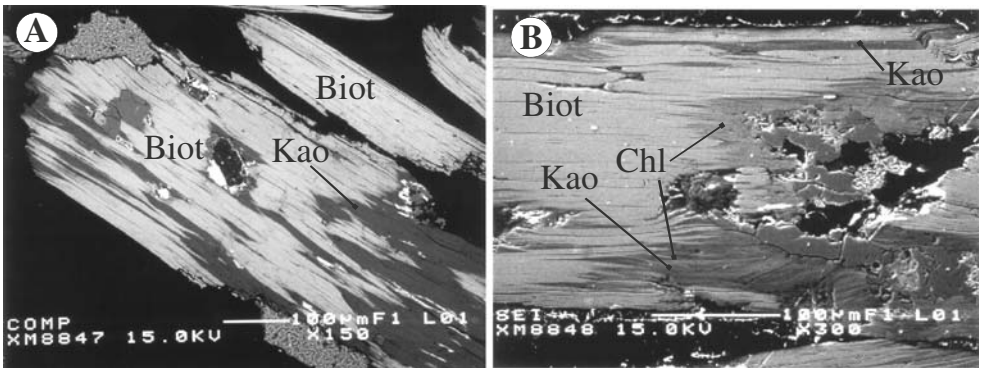

Fig. 3 Scanning electron microscope image of biotite phenocrysts altered to kaolinite (**a**) and kaolinite and chlorite (**b**). *Bio* biotite, *Kao* kaolinite, *Chl* chlorite

for this set of samples is 36.5 Ma, similar to the weighted mean age of all samples 36.6±0.5 Ma.

Fission track dating

Damage in the crystal lattice consisting of fission tracks are not stable and tends to be repaired naturally as a result of annealing. Several geological factors such as high temperature, pressure, and highly ionizing irradiation may be responsible for annealing, but according to Fleischer and Price (1964) and Fleischer et al. (1965), temperature is the only relevant factor under geologically reasonable conditions. The thermal annealing process is reported to occur at nonlinear rates that vary for different temperatures ranges and cooling rates (Green et al. 1986). The nominal temperature below which a fission track is effectively retained is defined as the closure temperature. Above this temperature, tracks undergo total restoration in a geological time scale, while below it, only progressive reduction in their initial length occurs.

Experimental data show that there is a wide range of temperature from 160°C to 380°C for zircon partial annealing, which is strongly dependent on cooling rates.

Table 1 Representative electron microprobe analysis of biotite phenocrysts

Sample	S-03	S-05	S-06	S-11	S-16	S-30	S-40
SiO_2	38.98	37.27	37.80	36.29	37.65	39.75	37.40
TiO_2	4.11	4.14	3.93	4.13	3.52	4.12	4.22
Al_2O_3	14.13	14.56	14.58	13.84	14.33	13.67	14.58
FeO	12.42	13.88	14.27	13.79	11.80	11.82	14.43
MgO	12.53	14.73	14.43	13.98	16.11	13.10	14.01
ZnO	0.00	0.02	0.00	0.00	0.05	0.01	0.00
CaO	0.08	0.03	0.00	0.02	0.00	0.09	0.02
Na_2O	1.24	0.19	0.21	0.23	0.46	0.12	0.20
K_2O	8.07	9.17	9.40	7.84	8.90	8.15	9.22
BaO	0.32	0.54	0.30	0.51	0.62	0.32	0.74
F	0.73	0.67	0.72	0.71	1.25	0.83	0.63
Cl	0.20	0.25	0.23	0.21	0.20	0.23	0.23
Total	92.80	95.45	95.87	91.55	94.90	92.20	95.68

The range of closure temperature in natural systems for annealing of fission tracks in zircons is estimated between 240±30°C for cooling rates of ~10°C/m.y. (Hurford 1986; Tagami et al. 1996; Brandon et al. 1998) and 194±18°C for cooling rates of 0.46°C/m.y. (Bernet et al. 2002). Effective annealing temperature of 240±30°C is considered as the most suitable value for the geological setting of the Zaldívar deposit.

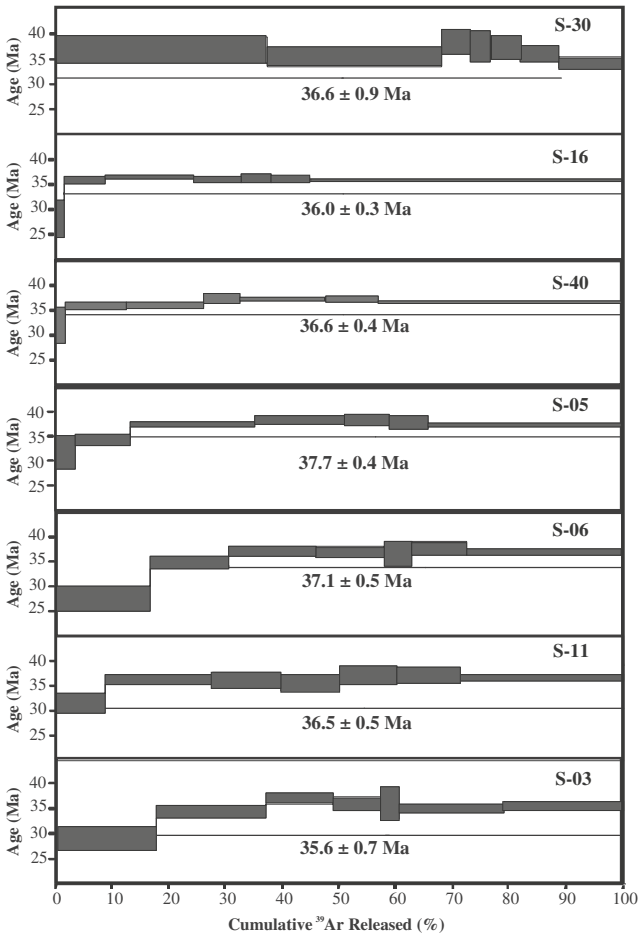

Fig. 4 $^{40}Ar/^{39}Ar$ age spectra. The plateau steps (2σ error) are indicated

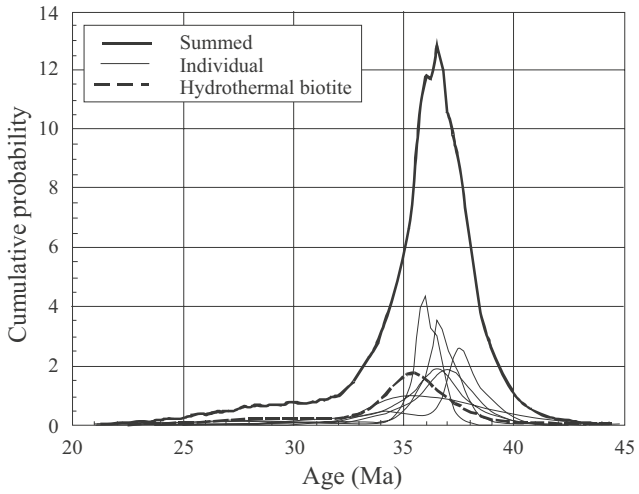

Fig. 5 Cumulative probability plot of step-heating biotite $^{40}Ar/^{39}Ar$ ages from the Llamo porphyry. The enveloping curve is generated by summing the probability curves for each individual sample. *Dotted line* represents the hydrothermal biotite (35.6±0.7 Ma) and is not included in the summed cumulative probability plot

Analytical results of fission track dating of single zircon grains on samples from LLP (S-03 and S-11), the andesites (S-13), and the ZP (S-23) (see Fig. 9) are presented in Table 2 and are also graphically illustrated in the form of radial plots (Fig. 6). The calculated average ages for all samples are concordant and range between 28.0±1.5 (2σ; S-11) and 29.9±1.8 Ma (2σ; S-23; Table 3; Fig. 6). The weighted average age of all samples is 29.1±1.7 Ma (2σ).

Fluid inclusion thermometry

Fluid inclusions, as in most porphyry copper deposits, are ubiquitous and abundant in most quartz veins. A detailed petrographic examination at room temperature allowed the identification of three major types of fluid inclusions. B-type inclusions consist of an aqueous fluid, a vapor bubble, and a halite crystal. Some of these inclusions may also contain other daughter mineral such as sylvite, hematite, and, less frequently, anhydrite. The dissolution temperature of halite crystals yielded salinity values between 30 and 56 wt.% NaCl equivalents (Fig. 7). About 30% of the fluid inclusions in this population homogenized with bubble disappearance at temperatures between 320°C and 495°C. In the other, 70% homogenization was attained by halite dissolution at 325°C to 500°C (Fig. 7)

G-type inclusions are low-salinity, low-density, and gas-rich inclusions, in which the vapor bubble comprises more than 60% of the volume and is surrounded by a thin rim of aqueous fluid. In some inclusions, hematite and anhydrite may also be present as daughter minerals. Raman spectroscopy analysis showed that some of these inclusions contain traces of CO_2 (<1 vol.%). Supercooling of G-type inclusions has no effect on the gas bubble, and the small amount of liquid made it difficult to distinguish changes in the liquid phase upon freezing. Nevertheless, it was possible to determine final ice melting temperatures between −0.4°C and −14°C, which corresponds to salinities of 0.35% to 17.3% NaCl equivalents. Final homogenization occurred to the vapor phase within a temperature range of 340°C to 463°C (Fig. 7).

W-type inclusions are low-salinity, liquid-rich inclusions on which final melting of ice after cooling between 0°C and −18°C, which corresponds to salinities from 0.0 to 20.7 NaCl wt.% equivalents. On further heating, the gas bubble disappeared into the liquid phase defining a final homogenization temperature between 221°C and 290°C (Fig. 7)

B- and G-types are genetically related, closely associated and may occur in linear arrays, randomly distributed, or in resealed microfractures within the host crystal. The G and B-type inclusions constitute about 40% of all observed fluid inclusions each. W-type inclusions occur along healed microfracture planes that frequently cut across the host crystal and represent about 20% of all observed inclusions.

Discussion

The hydrothermal system at the Zaldívar deposit is well characterized by abundant B-type (high salinity) and G-type vapor-rich aqueous fluid inclusions that homogenize at similar temperatures (320°C to 500°C and 340°C and 463°C, respectively). Because B- and G-type inclusions coexist and homogenize within the same temperature range (to liquid and vapor, respectively), we conclude that these inclusions were trapped along the immiscible surface of a boiling fluid system (Pichavant et al. 1982). When a fluid system is at boiling conditions, no pressure correction is required and the homogenization temperature is equal to the trapping temperature (Roedder 1984); hence, in this case, the trapping temperature is estimated between approximately 320°C and 495°C. Furthermore, if we consider that the compositions of these two coexisting types of fluid inclusions (types B and G) vary from 30 to 50 wt.% NaCl equivalents in the high salinity type and from 0.35 to about 10 wt.% NaCl equivalents in the G-type, then the fluid pressure at the immiscibility surface of the NaCl-H_2O system would be between 150 and 300 bars (Atkinson 2002) equivalent to 1,500 and 3,000 m in hydrostatic conditions or 560 to 1,130 m under purely lithostatic pressure (Shepherd et al. 1985). The overall composition of the postmagmatic aqueous fluids evolved from a complex Na–K–Fe–H_2O to a more simple NaCl-H_2O system (Campos et al. 2002).

Table 2 $^{40}Ar/^{39}Ar$ incremental heating data

Laser power (W)	$^{36}Ar_{(a)}$	$^{37}Ar_{(Ca)}$	$^{38}Ar_{(Cl)}$	$^{39}Ar_{(K)}$	$^{40}Ar_{(r)}$	$^{40}Ar_{(r)}$ (%)	$^{39}Ar_{(K)}$ (%)	K/Ca±2σ	Age±2σ (Ma)
Biotite S-03									
0.3	0.06277	0.00000	0.00197	0.66904	3.66048	16.48	17.28	0.000±0.000	29.05±2.39
0.5	0.02415	0.00000	0.00186	0.75225	4.88570	40.64	19.43	0.000±0.000	34.43±1.26
0.7	0.01021	0.13920	0.00145	0.45970	3.20875	51.53	11.87	1.420±2.946	36.98±1.04
0.9	0.00654	0.00000	0.00076	0.32375	2.19277	53.14	8.36	0.086±0.000	35.89±1.34
0.11	0.00228	0.11423	0.00040	0.13215	0.89879	57.19	3.41	0.497±1.280	36.04±3.26
0.14	0.01497	0.25379	0.00179	0.70985	4.67663	51.38	18.33	1.203±1.260	34.92±0.83
Fusion	0.01628	0.36533	0.00132	0.82557	5.54032	53.52	21.32	0.972±0.838	35.57±0.74
Σ	0.13721	0.87254	0.00955	3.87232	25.06343				
Age plateau S-03=35.6±0.7 Ma									
Biotite S-05									
0.3	0.00552	0.00000	0.00035	0.16469	0.98841	37.71	3.45	0.000±0.000	31.84±3.41
0.5	0.00441	0.00000	0.00168	0.46869	3.03083	69.92	9.83	0.000±0.000	34.29 ±1.10
0.7	0.00192	0.00000	0.00263	1.04929	7.42359	92.88	22.00	0.000±0.000	37.48±0.52
0.9	0.00035	0.00000	0.00141	0.75233	5.45756	98.14	15.77	0.000±0.000	38.42±0.77
0.11	0.00023	0.00000	0.00079	0.37841	2.74041	97.56	7.93	0.000±0.000	38.35±1.20
0.14	0.00027	0.00000	0.00053	0.32326	2.31178	96.71	6.78	0.000±0.000	37.88±1.42
Fusion	0.00091	0.00000	0.00347	1.63268	11.55998	97.70	34.23	0.000±0.000	37.51±0.39
Σ	0.01362	0.00000	0.01086	4.76935	33.51256				
Age plateau S-05=37.7±0.4 Ma									
Biotite S-06									
0.3	0.04574	0.00000	0.00264	0.63467	3.28383	19.54	16.60	0.000±0.000	27.48±2.43
0.5	0.01684	0.00000	0.00102	0.53137	3.49589	41.26	13.90	0.000±0.000	34.88±1.26
0.7	0.00915	0.00000	0.00132	0.58669	4.11629	60.35	15.35	0.000±0.000	37.17±1.03
0.9	0.00674	0.00000	0.00086	0.46703	3.25819	62.05	12.22	0.000±0.000	36.96±1.04
0.11	0.00337	0.00000	0.00022	0.17936	1.23849	55.46	4.69	0.000±0.000	36.59±2.55
0.14	0.00497	0.13040	0.00091	0.36978	2.62771	64.15	9.67	1.219±2.670	37.64±1.34
Fusion	0.01910	0.13243	0.00280	1.05397	7.35499	56.57	27.57	3.422±7.393	36.97±0.73
Σ	0.10592	0.26283	0.00977	3.82288	25.37539				
Age plateau S-06=37.1±0.5 Ma									
Biotite S-11									
0.3	0.00391	0.18056	0.00073	0.23523	1.39924	54.78	8.47	0.560±0.835	31.56±2.05
0.5	0.00115	0.38408	0.00085	0.52527	3.59748	91.36	18.91	0.588±0.488	36.29±1.05
0.7	0.00076	0.00000	0.00067	0.33917	2.31375	91.19	12.21	0.000±0.000	36.15±1.73
0.9	0.00072	0.20923	0.00065	0.28292	1.90097	89.95	10.19	0.581±0.891	35.61±1.68
0.11	0.00019	0.00000	0.00020	0.28573	2.00535	97.23	10.29	0.000±0.000	37.18±1.82
0.14	0.00005	0.00000	0.00071	0.31076	2.17556	99.27	11.19	0.000±0.000	37.09±1.67
Fusion	0.00019	0.00000	0.00101	0.79863	5.51729	98.96	28.75	0.000±0.000	36.60±0.59
Σ	0.00697	0.77387	0.00482	2.77772	18.90964				
Age plateau S-11=36.5±0.5 Ma									
Biotite S-16									
0.3	0.00718	0.05257	0.00036	0.14767	0.77867	26.86	1.35	1.208±6.531	28.01±3.75
0.5	0.01155	0.00000	0.00210	0.79596	5.39028	61.23	7.28	0.003±0.000	35.89±0.77
0.7	0.00423	0.24800	0.00390	1.71587	11.82169	90.43	15.69	2.975±3.446	36.51±0.33
0.9	0.00102	0.08450	0.00226	0.91170	6.19494	95.37	8.33	4.640±18.117	36.01±0.57
0.11	0.00047	0.00000	0.00118	0.57558	3.93791	96.56	5.26	0.001±0.000	36.25±0.83
0.14	0.00062	0.10278	0.00128	0.75398	5.13035	96.56	6.89	3.154±9.268	36.06±0.66
Fusion	0.00201	0.49444	0.01187	6.03769	40.86561	98.55	55.20	5.251±2.917	35.87±0.17
Σ	0.02707	0.98230	0.02295	10.93845	74.11945				
Age plateau S-16=36.0±0.3 Ma									
Biotite S-30									
0.3	0.11942	31.67767	0.00864	1.62172	11.28032	24.22	37.08	0.022±0.003	36.85±2.63
0.5	0.08559	0.00000	0.00361	1.35154	9.03506	26.32	30.90	0.000±0.000	35.43±1.88
0.7	0.00457	0.00000	0.00072	0.22017	1.59249	54.12	5.03	0.000±0.000	38.31±2.46
0.9	0.00399	0.00000	0.00000	0.16034	1.13647	49.10	3.67	0.000±0.000	37.55±3.13
0.11	0.00613	0.00494	0.00070	0.23312	1.64182	47.55	5.33	20.283±1334.625	37.31±2.31
0.14	0.00784	0.05353	0.00069	0.29602	2.01077	46.45	6.77	2.378±12.498	36.00±1.54
Fusion	0.01281	0.00000	0.00177	0.49095	3.16846	45.57	11.22	0.005±0.000	34.22±1.09
Σ	0.24034	31.73614	0.01614	4.37387	29.86539				

Table 2 (continued)

Laser power (W)	$^{36}Ar_{(a)}$	$^{37}Ar_{(Ca)}$	$^{38}Ar_{(Cl)}$	$^{39}Ar_{(K)}$	$^{40}Ar_{(r)}$	$^{40}Ar_{(r)}$ (%)	$^{39}Ar_{(K)}$ (%)	K/Ca±2σ	Age±2σ (Ma)
Age plateau S-30=36.6±0.9 Ma									
Biotite S-40									
0.3	0.00382	0.00000	0.00044	0.13690	0.82560	42.23	1.66	0.000±0.000	31.99±3.65
0.5	0.00420	0.05084	0.00208	0.88879	6.01176	82.89	10.80	7.517±40.076	35.85±0.71
0.7	0.00260	0.00000	0.00236	1.12720	7.68339	90.90	13.69	0.000±0.000	36.12±0.59
0.9	0.00030	0.30355	0.00096	0.53042	3.74539	97.68	6.44	0.751±0.706	37.41±0.97
0.11	0.00224	0.04366	0.00249	1.24023	8.70670	92.91	15.07	12.216±96.725	37.19±0.44
0.14	0.00084	0.17855	0.00194	0.76658	5.37868	95.56	9.31	1.846±3.069	37.17±0.60
Fusion	0.00191	0.00000	0.00745	3.54164	24.42302	97.73	43.02	0.005±0.000	36.54±0.23
Σ	0.01591	0.57660	0.01773	8.23176	56.77455				
Age plateau S-40=36.6±0.4 Ma									

J value=0.002967

$^{36}Ar_{(a)}$ atmospheric component in ^{36}Ar, $^{37}Ar_{(Ca)}$ calcium-derived ^{37}Ar, $^{38}Ar_{(Cl)}$ chlorine-derived component in ^{38}Ar, $^{39}Ar_{(K)}$ potassium-derived component in ^{39}Ar, $^{40}Ar_{(r)}$ sum of radiogenic and atmospheric components in ^{40}Ar, $^{40}Ar_{(r)}$ *(%)* percentage radiogenic component in ^{40}Ar, $^{39}Ar_{(K)}$ *(%)* increment size expressed as the percentage of $^{39}Ar_K$ compared to the total amount of $^{39}Ar_K$ released during the experiment, *K/Ca* molar K/Ca ratio

The latest hydrothermal event observed in the studied samples is characterized by low temperature (approximately 220°C to 290°C) low salinity (less than 10 wt.% NaCl equivalents) fluids. Previous U–Pb ages published by Richards et al. (1999) of zircons from the LLP at Zaldívar deposit (38.7±1.3 Ma, 2σ) and of the Escondida porphyry (37.9±1.1 Ma, 2σ) in the neighboring Escondida deposit indicate that the porphyry intrusions most closely related to mineralization were emplaced at approximately 38 Ma in both deposits (Richards et al. 1999).

The mineral ages determined by argon–argon incremental heating are within error of the U–Pb ages of Zaldívar, with $^{40}Ar/^{39}Ar$ ages of magmatic biotite between 36 and 38 Ma. The plateau ages obtained and the consistency of the data indicate that the Ar isotopic system has not been disturbed by postcrystallization events (i.e., resetting by late thermal events) and that the ages represent the time at which the system was closed to argon diffusion. All samples define a weighted average age of 36.6±0.5 Ma and are within error of previously published less precise

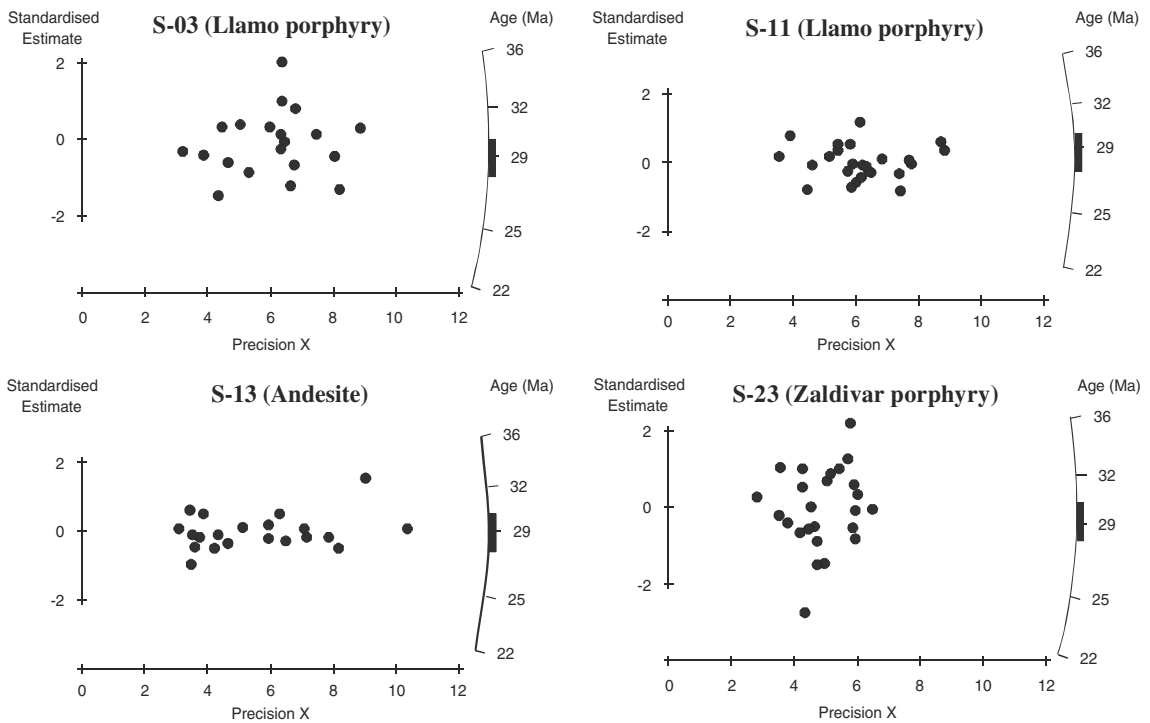

Fig. 6 Radial plot of fission track single grain ages (Galbraith 1990) in which the *y*-axis represents the standardized error, *x*-axis the precision, and the curved axis the central age in Ma

Table 3 Zircon fission track analytical results

Sample	Rock unit	N (grains)	ρ_s (cm^{-2}) ×10^6	N_s	ρ_i (cm^{-2}) ×10^6	N_i	ρ_d (cm^{-2}) ×10^6	N_d	P (χ^2)	Disper sion	Central age Ma±2σ
S-03	Llamo	20	4.63	1,486	10.35	1,661	0.66	13,724	80.5	9	29.6±1.8
S-11	Llamo	25	4.10	1,839	9.70	2,173	0.66	13,724	99.9	5	28.0±1.5
S-13	Andesite	21	2.94	1,399	6.67	1,588	0.66	13,724	99.9	5	28.9±1.8
S-23	Zaldívar	25	3.27	1,189	7.23	1,313	0.66	13,724	31.1	12	29.9±1.8

Central ages were calculated using the Zeta-methods; ζ value for CN-2 glass (P. Andriessen)=100.3±2.99

magmatic biotite $^{40}Ar/^{39}Ar$ age of 37.4±1.8 Ma (Richards et al. 1999).

In contrast to the magmatic biotite, hydrothermal biotite from sample S-03 and S-16 (Fig. 8) yielded somewhat younger ages (Fig. 4). The younger age of 35.6±0.7 Ma of sample S-03 can be explained by the fine-grained nature of the biotite more prone to Ar diffusion, whereas the younger age of 36.0±0.3 Ma of sample S-16 is probably related to chemical disturbances related to kaolinitization. This indicates that alteration may have disturbed the $^{40}Ar/^{39}Ar$ systematics in some other samples as well and that it is necessary to evaluate to what extent this phenomena could have affected the final outcome of the ages in the context of the hydrothermal alteration observed in the analyzed samples.

All studied samples are clearly affected by potassic alteration (which occurs at temperatures between 350–700°C; Titley and Beane 1981) but show no evidence of being affected by lower temperature hydrothermal alteration types, such as phyllic or propylitic alteration. The potassic alteration is overprinted by the supergene alteration characterized by kaolinitization of biotite and feldspars. Kaolinite is not stable at temperatures higher that 300°C (Henley and McNabb 1978; Moore and Nash 1974). Since the closure temperature of biotite for the $^{40}Ar/^{39}Ar$ system in a relatively fast cooling system (100°C/Ma) is around 300±50°C (Harrison et al 1985), below the minimum temperature for potassic alteration and above the temperature at which kaolinite is stable, the only perturbation on the $^{40}Ar/^{39}Ar$ system that may be expected would be of chemical nature related to the kaolinitization of biotite produced by supergene fluids.

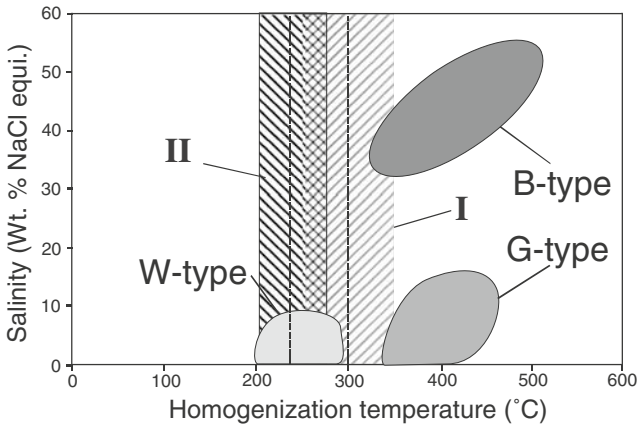

Fig. 7 Homogenization temperature–salinity fields defined by the studied fluid inclusions. *B-type* (high salinity fluids), *G-type* (gas-rich, low-salinity fluids), *W-type* (liquid-rich, low salinity fluids), *I* (closure temperature of biotite for the $^{40}Ar/^{39}Ar$ system, 300±50°C), *II* (annealing temperature for fission tracks in zircons, 240±30°C)

The biotite ages from the Zaldívar porphyry copper system confirm the temporal relationship with other porphyry copper deposits related to the Domeyko Fault System in northern Chile (e.g., Chuquicamata, Collahuasi, El Salvador) on which current information indicates an age range of 42 to 31 Ma (Late Eocene–Early Oligocene) for mineralization (e.g., Richards et al. 1999; Camus 2003). Because the $^{40}Ar/^{39}Ar$ ages of biotite reflect the time at which the samples were cooled below 300°C, the closure temperature is useful to constrain the cessation of the high temperature hydrothermal system, which at the Zaldívar deposit was constrained by fluid inclusion thermometry having been active at temperatures above 320°C.

All samples selected for zircon fission track thermochronology (S-03, S-11, S-13, and S-23) independent of their provenance (sample S-03 was collected east of the Portezuelo fault and sample S-11 west of this fault; Fig. 8) or the host rock of the zircon grains (andesites: sample S-13; Llamo porphyry: samples S-03 and S-11; ZP: sample S-23; Fig. 8) yielded comparable ZFT ages of approximately 29 Ma (the weighted mean age of all ZFT ages is 29.1±1.2 Ma). This indicates that the postmineral thermal effects both sides of the Portezuelo fault and the ages represent cooling of the entire area and not exhumation controlled by fault movement.

The application of ZFT dating to this type of hydrothermal system is particularly useful in constraining the time at which the geothermal gradient cooled off. At the Escondida deposit (coeval with and only 5 km south of Zaldívar deposit), magmatic activity continued long after the main mineralization event and is represented by a suite of dacitic dikes that yielded ages as young as 31 Ma (K–Ar whole-

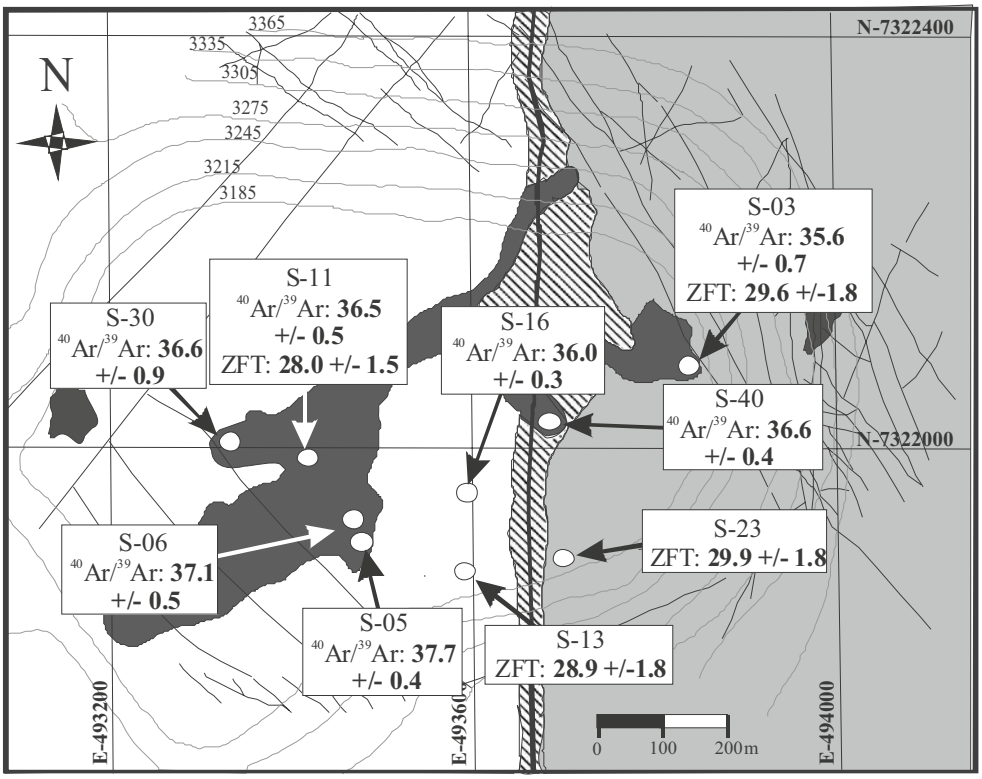

Fig. 8 Distribution of $^{40}Ar/^{39}Ar$ dating in biotite and zircon fission track ages on the Zaldívar deposit

rock; Alpers and Brimhall 1988). This value is within error of the ZFT age of 29.1±1.2 Ma defined at Zaldívar; however, no direct evidence of postmineralization magmatic activity has been found at Zaldívar. Because ZFT data signal the cooling under the ZFT closure temperature, ZFT ages most probably date the end of the thermal activity in the Zaldívar–Escondida area, i.e., the time when the whole area cooled below a temperature of approximately 240°C (Fig. 9). The time for cessation of the thermal activity

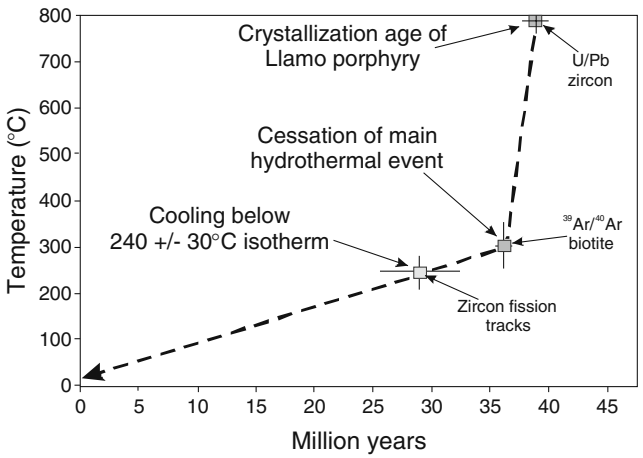

Fig. 9 Thermal and temporal evolution on the Zaldívar porphyry copper deposit

constrained by the ZFT may be related to the cooling of the low temperature hydrothermal pulse, between 220°C and 300°C as defined by fluid inclusion thermometry.

Conclusions

The U–Pb crystallization age of the Llamo porphyry (38.7± 1.3 Ma; Richards et al. 1999) in combination with $^{40}Ar/^{39}Ar$ thermochronology of biotite and zircon fission track dating together with fluid inclusion microthermometry data obtained in the present study allows us to put constraints on the thermal evolution of the Zaldívar porphyry copper system (Fig. 9). Fluid inclusion microthermometry has defined two principal hydrothermal stages in the Zaldívar deposit. The first event characterized by coexisting magmatic brine and vapor having homogeneization temperatures between 320°C and 495°C. The second stage is characterized for low-salinity, low-temperature (mostly between 221°C and 300°C) aqueous fluids, most probably related to a mixture of magmatic water and heated groundwater.

The biotite $^{40}Ar/^{39}Ar$ ages are consistent and yielded a weighted average of 36.6±0.5 Ma. This age is slightly younger and almost overlaps within error with the U–Pb age for the Llamo porphyry. Hydrothermal biotites sample S-03

yielded slightly younger $^{40}Ar/^{39}Ar$ age (35.6±0.7 Ma) that also overlaps with weighted average of magmatic biotites. This younger age may be related to the fine-grained nature of the biotites, as grain size influences the closure temperature, and may not have a direct relationship with their magmatic versus hydrothermal origin.

As mentioned above, the earliest hydrothermal stage characterized by minimum temperatures of approximately 320°C, sufficient to release argon from biotites as is slightly higher than the closure temperature for the $^{40}Ar/^{39}Ar$ system in biotites. Thus, the ages would indicate that the main hydrothermal system related to the Llamo porphyry cooled below the closure temperature of the $^{40}Ar/^{39}Ar$ system shortly after crystallization of the intrusion. In fact, the time span between the crystallization age of the Llamo porphyry and the cessation of the main mineralization–alteration event is 1.5 m.y. or less (Fig. 9), confirming a close temporal connection between crystallization of the parent intrusion and the development of the hydrothermal system responsible of the mineralization–alteration; a similar feature has been observed for other porphyry copper deposits of northern Chile (e.g., Reynolds et al. 1997; Clark et al. 1998; Richards et al. 1999).

Finally, because fission tracks produced in zircons are only retained at temperatures lower than about 240±30°C, the similar ZFT ages in all studied samples, independent of the nature of the host rock (i.e., andesites, or porphyries) or the location of samples with respect to the Portezuelo fault, indicate that the whole area cooled below that temperature about 29 Ma ago (Fig. 9), in agreement with youngest published ages for Escondida deposit.

Acknowledgments We gratefully acknowledge Compañía Minera Zaldívar for providing field support and access to the mine and to unpublished reports; special thanks are owed to Jaime Delgado and Patricio Morales. Facilities for all analytical work were provided by the Vrije Universiteit Amsterdam, The Netherlands. Comprehensive and thoughtful reviews by T. Bissig, A. Harris, and V. Maksaev on the original manuscript provided numerous suggestions that significantly improve the content and clarity of this paper; we want to express our thanks for their interest. We also acknowledge the excellent editorial comments from Patrick Williams and Lawrence Meinert. Finally thanks also to L. Kerstein and F. Barra for the comments aimed at enhancing readability of the final text.

References

Alpers HC, Brimhall GH (1988) Middle Miocene climatic change in the Atacama Desert, northern Chile: evidences from supergene mineralization at La Escondida. Geol Soc Amer Bull 100:1640–1656

Atkinson AB (2002) A model for the PTX properties of H_2O-NaCl. Ph.D. thesis, Virginia Polytechnic Institute and State University

Brandon MT, Roden-Tice MK, Garver JI (1998) Late Cenozoic exhumation of the Cascadia accretionary wedge in the Olympic mountains, northwest Washington State. Geol Soc Amer Bull 110:985–1009

Bernet M, Brandon MT, Garver JI, Reiners PW, Fitzgerald PG (2002) Determining the zircon fission-track closure temperature. Geol Soc Amer 34:18

Boric R, Diaz F, Maksaev V (1990) Geología y yacimientos metalíferos de la Región de Antofagasta. Boletín No 40, Servicio Nacional de Geología y Minería

Burnham CW (1979) Magmas and hydrothermal fluids. In: Barnes HL (ed) Geochemistry of hydrothermal ore deposits. 2nd edn. Wiley, New York, pp 71–136

Campos E, Touret JLR, Nikogosian I, Delgado J (2002) Overheated, Cu-bearing magmas in the Zaldívar porphyry-Cu deposit, Northern Chile. Geodynamic consequences. Tectonophysics 345:229–251

Camus F (2003) Geología de los sistemas porfídicos en los Andes de Chile. Servicio Nacional de Geología y Minería, Santiago, Chile 267 p

Clark AH, Archibald DA, Lee AW, Farrar E, Hodgson CJ (1998) Laser probe $^{40}Ar/^{39}Ar$ ages of early- and late-stage alteration assemblage, Rosario porphyry copper–molybdenum deposit, Collahuasi District, I Region, Chile. Econ Geol 93:326–337

Candela PA, Piccoli PM (2005) Magmatic processes in the development of porphyry-type ore systems. Econ Geol One Hundred Anniversary Volume, pp 25–38

Cline JS (1995) Genesis of porphyry copper deposits: the behavior of water, chloride, and copper in crystallizing melts. Ariz Geol Soc Dig 20:69–82

Cline JS (2003) How to concentrate copper. Science 302:2075–2076

Cooke DR, Hollings P, Walshe JL (2005) Giant porphyry deposit: characteristics, distribution, and tectonic controls. Econ Geol 100:801–818

De Bruijne CH (2001) Denudation, intraplate tectonics and far field effects; and integrated apatite fission track study in central Spain: Ph.D. thesis, Vrije Universiteit Amsterdam, p 164

Deckart K, Clark AH, Aguilar AC, Vargas RR, Bertens NA, Mortensen JK, Fanning M (2005) Magmatic and hydrothermal chronology of the giant Río Blanco porphyry copper deposit, central Chile, implications of an integrated U–Pb and $^{40}Ar/^{39}Ar$ database. Econ Geol 100:905–934

Einaudi MT (1998) Porphyry copper and epithermal systems. Short course. Instituto de Geología Económica Aplicada, Universidad de Concepcion, Chile

Fleischer RL, Price PB (1964) Techniques for geological dating of minerals by chemical etching of fission fragments tracks. Geochim Cosmochim Acta 28:1705–1714

Fleischer RL, Price PB, Walker RM (1965) Effects of temperature, pressure and ionization on the formation and stability of fission tracks in minerals and glasses. J Geophys Res 70:1497–1502

Fournier R (1999) Hydrothermal processes related to movement of fluid from plastic into brittle rock in the magmatic–epithermal environment. Econ Geol 94:1193–1212

Galbraith RF (1990) The radial plot: graphical assessment of spread in ages. Nucl Tracks Radiat Meas 17:207–214

Green PF, Duddy IR, Gleadow AWJ, Tingate PR, Laslett GM (1986) Thermal annealing of fission tracks in apatite, 1: a qualitative description. Chem Geol 59:237–253

Gow PA, Walsh JL (2005) The role of preexisting geologic architecture in the formation of giant porphyry-related Cu ± Au deposit: examples from new Guinea and Chile. Econ Geol 100:819–834

Harris AC, Kamenetsky V, White NC, van Achterbergh E, Ryan CG (2003) Melt inclusions in veins: linking magma and porphyry Cu deposits. Science 302:2109–2111

Harris AC, Golding SD, White NC (2005) The genesis of Bajo de la Alumbrera deposit: stable isotope evidence for a porphyry-related

hydrothermal system dominated by magmatic aqueous fluids. Econ Geol 101:71–94

Harris AC, Dunlap WJ, Reiners PW, Allen CM, Cooke DR, White NC, Campbell IH, Golding SD (2007) Multimillion year history of a porphyry copper deposit: application of U–Pb, $^{40}Ar/^{39}Ar$ and (U–Th)/He chronometers, Bajo de la Alumbrera copper-gold deposit, Argentina. Miner Depos 43:295–314

Harrison TM, Duncan I, McDougall I (1985) Diffusion of ^{40}Ar in biotite: temperature, pressure and compositional effects. Geochim Cosmochim Acta 49:2461–2468

Henley RW, McNabb A (1978) Magmatic vapor plumes and groundwater interaction in porphyry copper emplacement. Econ Geol 59:538–569

Hurford AJ (1986) Cooling and uplift pattern in the Lepontine Alps, South Central Switzerland and an age of vertical movement on the Insubric fault line. Contrib Mineral Petrol 92:413–427

Maksaev V, Munizaga F, Mc Williams M, Fanning M, Marthur R, Ruiz J, Zentilli M (2004) New chronology for El Teniente, Chilean Andes, from U–Pb, $^{40}Ar/^{39}Ar$, Re–Os, and fission track dating implications for the evolution of a supergiant porphyry Cu–Mo deposit, Chile. Econ Geol Spec Publ 11:15–54

Marinovic N, Smoje I, Maksaev V, Herve M, Mpodozis C (1995) Hoja Aguas Blancas, Región de Antofagasta: Servicio Nacional de Geología y Minería. Carta Geol Chile 70:150

Maturana M, Zaric N (1991) Geología y mineralización del yacimiento tipo pórfido cuprífero Zaldívar, en los Andes del Norte de Chile. Rev Geol Chile 18:109–120

Moore WJ, Nash JT (1974) Alteration and fluid inclusion studies of the porphyry copper ore body at Bingham, Utah. Econ Geol 69:631–645

Ojeda JM (1986) Escondida porphyry copper deposit, II region, Chile: exploration drilling and current geological interpretation. Institution of Mining and Metallurgy (London) Mining Latin America Conference, Santiago, 17–19 November 1986, Papers, p 199–318

Padilla-Garza R, Titley SR, Eastoe CJ (2004) Hypogene evolution of the Escondida porphyry copper deposit, Chile. Society of Economic Geologist Special Publication 11, pp 141–165

Pichavant M, Ramboz C, Weisbrod A (1982) Fluid immiscibility in natural processes: use and misuse of fluid inclusion data. I. Phase equilibria analysis—a theoretical and geometrical approach. Chem Geol 37:1–27

Proffett JM (2003) Geology of the Bajo de la Alumbrera porphyry copper–gold deposit, Argentina. Econ Geol 98:1535–1574

Richards JP, Noble SR, Pringle M (1999) A revised late Eocene age for porphyry copper magmatism in the Escondida Area, Northern Chile. Econ Geol 94:1231–1248

Richards JP (2003) Tectono-magmatic precursors for porphyry Cu–(Mo–Au) deposit formation. Econ Geol 98:1515–1534

Reynolds P, Ravenhurst C, Zentilli M, Linsay D (1997) High precision $^{40}Ar/^{39}Ar$ dating of two consecutive hydrothermal events in the Chuquicamata porphyry copper system, Chile. Geological Association of Canada–Mineralogical Association of Canada, Program with abstracts 22, pp A-125

Roedder E (1984) Fluid inclusions. Rev Miner 12:1–644

Seedorff E, Dilles JH, Proffett JM, Einaudi MT, Zucher L, Stavast WJA, Johnson DA, Barton MD (2005) Porphyry deposits: characteristics and origin of hypogene features. Econ Geol One Hundred Anniversary Volume, pp 251–298

Shepherd T, Rankin AH, Alderton DHM (1985) A practical guide to fluid inclusion studies. Blakie, Glasgow, p 240

Tagami T, Carter A, Hurford AJ (1996) Natural long-term annealing of zircon fission-track system in the Vienna Basin deep borehole samples: constrains upon partial annealing zone and closure temperature. Chem Geol 130:147–157

Tagami T (2005) Zircon fission-track thermochronology and applications to fault studies. Rev Mineral Geochem 58:95–122

Titley SR, Beane RE (1981) Porphyry copper deposits. Part I: geologic settings, petrology, and tectonogenesis. Econ Geol 75th Anniversary, pp 214–249

Wijbrans JR, Pringle MS, Koppers AAP, Scheveers R (1995) Argon geochronology of small samples using the Vulkaan argon laserprobe. Proc Kon Ned Akad v Wetensch 98:185–218

William-Jones AE, Heinrich CA (2005) Vapor transport of meals and the formation of magmatic–hydrothermal ore deposits. Econ Geol 100:1285–1312

Zentilli M, Krogh T, Maksaev V, Alpers C (1994) Uranium–lead dating of zircons from Chuquicamata and La Escondida porphyry copper deposit, Chile: inherited zircon cores of Paleozoic age with Terciary overgrowths. Comunicaciones (Universidad de Chile) 45:101–110